ADVANCED ENERGY MATERIALS
www.advenergymat.de

Photoinduced Metastable Asymmetric Cu Single Atoms for Photoreduction of CO_2 to Ethylene

*Qingyu Wang, Yida Zhang, Minxi Lin, Hengwei Wang, Yu Bai, Chengyuan Liu, Junling Lu, Qiquan Luo, Gongming Wang, Hai-Long Jiang, Tao Yao, and Xusheng Zheng**

Metastable structures are promising candidates for efficient catalysis owing to abundant active electronic states, strong electronic coupling with reactants, and energetic preference. Exerting the value of metastable structures while evading the difficulty in direct synthesis remains challenging. Herein, it is reported that light irradiation enables the generation and maintenance of the metastable state over copper single atoms for efficient carbon dioxide reduction. Under irradiation with light, photogenerated electrons transit to Cu-3*d* orbits and initiate *d*-orbital rearrangement. The initial symmetric Cu_1—O_4 coordination converts to the metastable asymmetric structure of Cu_1—O_{2+1}, and is reversibly restored after removing the light. The photoinduced metastable intermediate of Cu_1—O_{2+1} promotes the Cu single-atom catalyst to deliver an ethylene yield rate of 60.4 µmol $g_{cat.}^{-1}$ h^{-1}. Mechanistic studies reveal that Cu_1—O_{2+1} possesses stronger adsorption capability for reactants and intermediates. The reaction energy barrier over Cu_1—O_{2+1} also shows an obvious decline compared to that over Cu_1—O_4.

1. Introduction

Metastable structures are ubiquitous in nature.[1,2] Compared with the thermodynamically stable ground-state, the metastable structures with relatively higher free energy possess unique physicochemical properties.[3–5] In virtue of abundant active electronic states, strong electronic coupling with reactants, and energetic preference in the reaction pathway, metastable materials have been extensively applied in the field of catalysis.[6–9] Unfortunately, the structures in a kinetically metastable state tend to ultimately convert to a lower-energy and thermodynamic equilibrium state. Currently, the synthesis of metastable structures mainly relies on high-energy or nonequilibrium strategies, including electron beam irradiation, hydrothermal reaction, and plasmonic hot electron.[10–12] For instance, Chun and co-workers utilized the hydrated electrons excited by the high-energy electron beam generated from transmission electron microscopy (TEM) to induce the generation of metastable hexagonal close-packed palladium hydride (PdH_x).[1] Zhang et al. fabricated metastable Ce–Zr oxides by igniting the precursor steam at ≈800 °C and subsequent rapid quenching.[13] In addition, the plasma oxidation with the electroreduction method was applied in the synthesis of metastable phase Cu.[14]

Instead of pursuing the direct synthesis of a metastable structure, we can just think out of the box for the in situ generation. Specifically, the catalysts may commonly exist in a thermodynamically stable form, but reconstruct into a high-energy metastable state induced by an external-field stimulation during the catalytic process. A similar concept has been already utilized as the pre-activation treatment in the conventional heterogeneous catalysis. However, the pre-activation is generally time-consuming while the storage of catalysts requires further surface passivation. Therefore, it would hold great application prospects to design a catalyst that enables reversible stable–to–metastable evolution during the reaction.

Herein, we realized and preserved the metastable state of the active structure by using an external light field. The light irradiation induced the conversion of copper (Cu) single atoms from symmetric coordination environment to asymmetric metastable one. Specifically, the photogenerated electron transition from TiO_2 to Cu rearranged the energy levels of Cu 3*d* orbits. As a result, the initial four-coordinated Cu_1—O_4 was distorted into Cu_1—O_{2+1} structure, namely twofold normal Cu—O coordination and one stretched Cu—O coordination. Moreover, Cu_1—O_4 was reversibly recovered after the removing the synergistic light field. Impressively, the distinctive metastable intermediate of

Q. Wang, Y. Zhang, C. Liu, T. Yao, X. Zheng
National Synchrotron Radiation Laboratory
University of Science and Technology of China
Hefei, Anhui 230029, China
E-mail: zxs@ustc.edu.cn

Q. Wang, Y. Zhang, H. Wang, J. Lu, G. Wang, H.-L. Jiang
College of Chemistry and Materials Science
University of Science and Technology of China
Hefei, Anhui 230026, China

M. Lin, Q. Luo
Institutes of Physical Science and Information Technology
Anhui University
Hefei, Anhui 230601, China

Y. Bai
Experimental Center of Engineering and Material Science
University of Science and Technology of China
Hefei, Anhui 230026, China

The ORCID identification number(s) for the author(s) of this article can be found under https://doi.org/10.1002/aenm.202302692

DOI: 10.1002/aenm.202302692

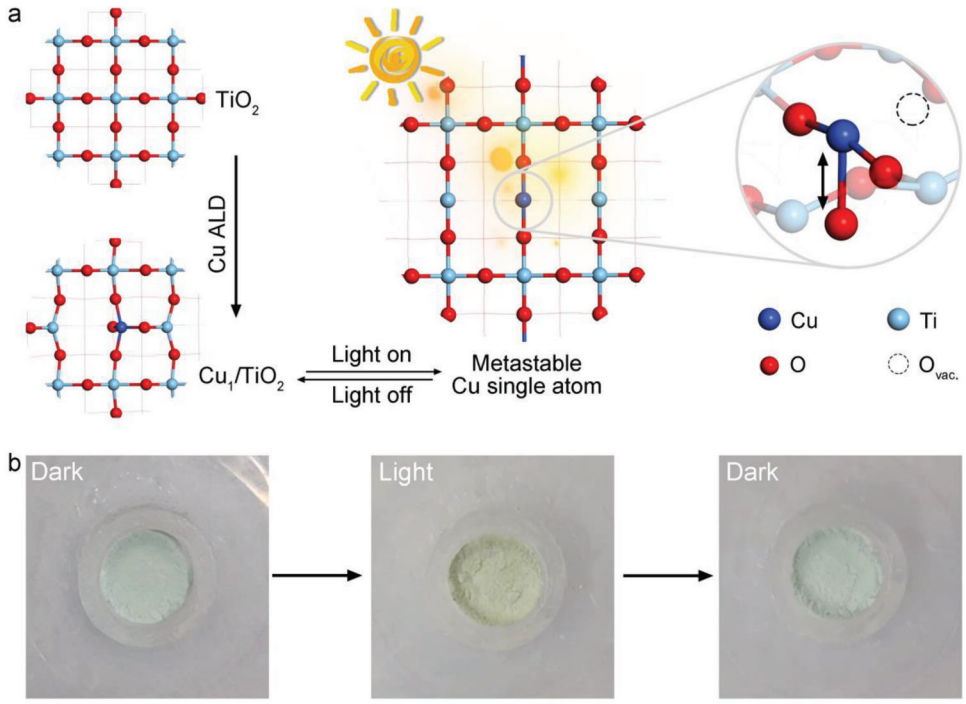

Figure 1. a) Scheme of the synthesis process of metastable Cu single atom. b) Photographs of Cu_1/TiO_2 in various situations.

$Cu_1—O_{2+1}$ under irradiation boosted the carbon dioxide (CO_2) reduction process. The yield rate of ethylene (C_2H_4) was up to 60.4 μmol $g_{cat.}^{-1}$ h^{-1} with the electron-based selectivity of 75.2%. Theoretical calculations indicate that $Cu_1—O_{2+1}$ structure enhanced the adsorption capability for reactant molecules, as well as remarkably lowered the reaction energy barrier. The asymmetrical metastable structure promotes the efficient activation and transformation of CO_2 molecules.

2. Results and Discussion

We synthesized atomically dispersed Cu atoms on TiO_2 nanosheets (denoted as Cu_1/TiO_2) via atomic layer deposition (ALD) method (**Figure 1**a; Figure S1–S3, Supporting Information). Interestingly, the color of the Cu_1/TiO_2 sample changed from wathet blue to chartreuse upon the stimulation of external light field and was recovered to wathet blue after removing the light (Figure 1b). In contrast, no change in the color of TiO_2 was captured under the same treatments (Figure S4, Supporting Information). Meanwhile, the same color of Cu_1/TiO_2 under different temperatures excluded the possibility that the photothermal effect arises the color variety (Figure S5, Supporting Information). As such, we inferred that a photoinduced reversible structural transformation occurred in Cu_1/TiO_2 where the new color corresponded to a newly generated metastable intermediate. To unveil this phenomenon, the basic properties of Cu_1/TiO_2 were first explored. The mass loading of Cu was determined as 0.41 wt.% by inductively coupled plasma atomic emission spectroscopy (ICP-AES). Furthermore, the magnified high-angle-annular-dark-field scanning transmission electron microscopy (HAADF-STEM) image with the corresponding intensity profile analysis indicates the isolated distribution of Cu atoms on TiO_2 nanosheets (Figure S6, Supporting Information). As displayed in the energy-dispersive X-ray (EDX) elemental mapping images of Cu_1/TiO_2, Cu, Ti, and O elements were homogeneously dispersed on the entire nanosheets (Figure S7, Supporting Information).

In order to further observe the electronic properties of the as-obtained samples, X-ray photoelectron spectroscopy (XPS) measurements were carried out. As shown in O 1*s* spectra of TiO_2, the peak at 530.1 eV was assigned to the lattice oxygen (Figure S8, Supporting Information).[15] For Cu_1/TiO_2, a new peak attributed to the oxygen vacancy arose at 531.9 eV.[16] Obviously, the introduction of Cu single atoms caused the disorders in the TiO_2 support through Jahn–Teller effect.[17] This point was verified by the presence of Ti^{3+} species in Cu_1/TiO_2 (Figure S9, Supporting Information).[18] Meanwhile, Cu 2*p* XPS profile of Cu_1/TiO_2 was recorded. The peaks at 934.7 and 954.7 eV were attributed to Cu^{2+}, while those at 932.9 and 952.9 eV were attributed to Cu^+ or Cu^0 species (Figure S10, Supporting Information).[19] X-ray absorption near-edge structure (XANES) and extended X-ray absorption fine structure (EXAFS) were conducted to determine the existence from of Cu species in Cu_1/TiO_2. As displayed in Cu K-edge XANES spectra, the absorption edge position of Cu_1/TiO_2 was close to that of CuO, implying the valence state of Cu species in Cu_1/TiO_2 was near +2 (Figure S11, Supporting Information). As depicted in the Fourier-transformed EXAFS (FT-EXAFS) in R space, the dominant peak was attributed to the nearest shell coordination of Cu—O bond, and the peak for Cu—Cu contribution at longer distance is absence (Figure S12, Supporting Information). The best fitting result for Cu_1/TiO_2 indicates that the major coordination peak was originated from

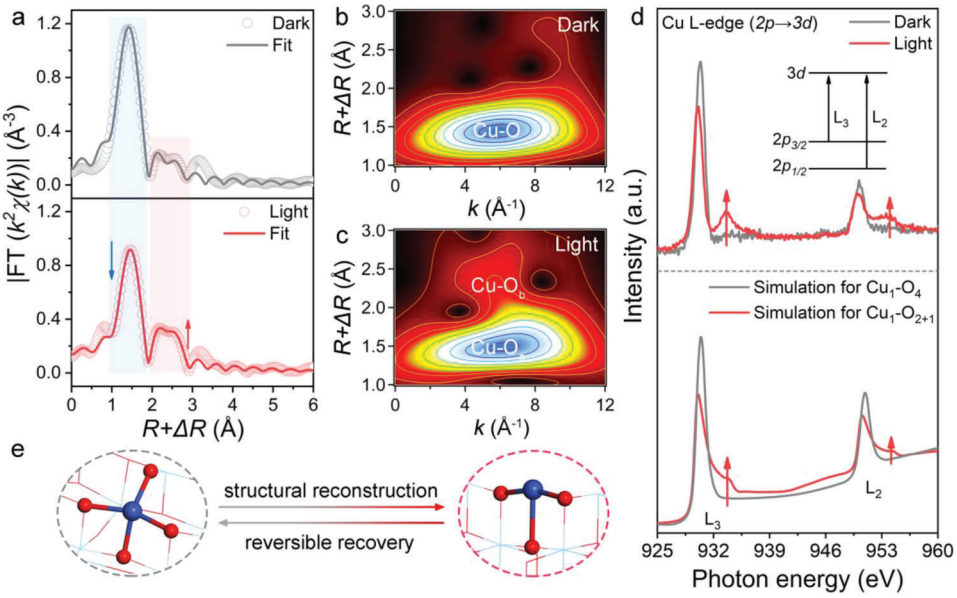

Figure 2. a) The Fourier transformed Cu K-edge spectra for Cu_1/TiO_2 under dark and light. b,c) Wavelet transform contour spectra of Cu K-edge EXAFS data for Cu_1/TiO_2 under dark and light. d) In situ Cu L-edge sXAS spectra for Cu_1/TiO_2 under dark and light (above). The theoretical data of Cu L-edge curves calculated with the depicted structures (below). e) Schematic illustration of the reversible structural conversion in Cu_1/TiO_2. The indigo, blue, and red spheres represent Cu, Ti, and O atoms, respectively.

the four Cu—O coordination with a mean Cu—O bond length of 1.94 Å (Figure S13 and Table S1, Supporting Information). Therefore, Cu species were in the atomical dispersion throughout TiO_2 nanosheets.

In addition, we explored the optical properties of Cu_1/TiO_2. As depicted in the diffuse reflectance ultraviolet-visible (UV–*vis*) diffuse reflectance spectra, Cu_1/TiO_2 exhibited the enhanced light-absorbing capability compared with that of TiO_2 (Figure S14, Supporting Information). Then, ultraviolet photoelectron spectroscopy was conducted to explore the energy band structure of the prepared samples (Figures S15 and S16, Supporting Information). Moreover, we investigated the carrier kinetics for the as-obtained catalysts. The decreased peak intensity of Cu_1/TiO_2 relative to that of TiO_2 in the room-temperature steady-state photoluminescence spectra indicates the inhibited carrier recombination (Figure S17, Supporting Information).[20] The enhanced photocurrent responses and the smaller semicircle in the electrochemical impedance spectra (EIS) indicate the inhibited carrier recombination and accelerated carrier-transfer kinetics in Cu_1/TiO_2, respectively (Figure S18, Supporting Information).[20,21]

Furthermore, we carried out in situ measurements to monitor the structural conversion in Cu_1/TiO_2. In situ XANES spectra at Cu K-edge were recorded under different conditions (Figure S19, Supporting Information). Relative to that under darkness, the absorption edge shifted to a lower energy under light, suggesting the partial reduction of $Cu^{\delta+}$ ($0<\delta<2$) to low-valence species. Meanwhile, in situ EXAFS was employed for tracking the atomic coordination structure evolution of Cu_1/TiO_2 under irradiation of light. For the FT-EXAFS curve under irradiation, the intensity of the coordination peak located at ≈2.0 Å distinctly declined, along with the intensified intensity of another peak at ≈2.4 Å (**Figure 2**a). Moreover, the wavelet transform (WT) analysis with the resolution in both R and *k* spaces of Cu K-edge EXAFS oscillations were carried out. The transverse axis represents wavevector, which is the key reference to distinguish the neighboring coordination atoms around the central atom (Figure 2b).[22] Generally, the contour maxima of light elements (e.g., C, N, and O atoms) are located at the low-*k* region, and vice versa.[23] Obviously, the WT-EXAFS contour plots of Cu_1/TiO_2 in dark exhibited only one intensity maximum at ≈5 $Å^{-1}$, which was assigned to the typical Cu—O coordination. When it comes to the case of being irradiated, a new center with the same *k* value of 5 $Å^{-1}$ but longer bond length was observed (Figure 2c). As such, the fact is that the isolated Cu single atoms were still coordinated with O atoms, but partial Cu—O bond was stretched. We further conducted EXAFS fitting analyses (Figure S20, Supporting Information). Compared with the pristine Cu_1/TiO_2, the symmetrically geometric configuration of the central Cu atom was destroyed upon light irradiation. The initial four-coordinated Cu_1–O_4 (R = 1.94 Å) changed into metastable Cu_1—O_{2+1} structure, namely twofold normal Cu—O coordination (R = 2.00 Å) plus one stretched Cu—O coordination (R = 2.35 Å).

We then turned to in situ soft X-ray absorption spectroscopy (sXAS) owing to the orbital transitions detected by soft X-ray is closely correlated to the photogenerated electron transition. In situ sXAS spectra under light were collected to explore the internal causes of the photo-induced metastable structure generation in Cu_1/TiO_2. As displayed in Ti L-edge spectra, the peaks for $2p_{3/2}\rightarrow 3d$ (L_3) and $2p_{1/2}\rightarrow 3d$ (L_2) transitions were in the range of 457–462 and 462–467 eV, respectively (Figure S21, Supporting Information).[24] Due to the existence of octahedral crystal field in the TiO_2 crystal, the Ti $L_{2,3}$ peaks further split into t_{2g} and e_g orbits, respectively.[25] As depicted in O K-edge spectra, the peaks at 531.2 eV and 533.9 eV were associated the electron excitation from 1*s* to the 2*p* state which was hybridized with t_{2g}

and e_g states in Ti 3*d* orbit, respectively (Figure S22, Supporting Information).[26] Under the irradiation of light, the intensity ratio of t_{2g}/e_g declined apparently, implying the generation of more oxygen vacancies.[27] It was correlated with the decrease of O atoms coordinated around the central Cu atom, consistent with in situ EAXFS analysis. As for Cu L-edge spectra, the peaks at 931.2 and 951.2 eV were attributed to the transition of $2p_{3/2}$ to 3*d* (L_3) and $2p_{1/2}$ to 3*d* (L_2), respectively (Figure 2d).[28] The absorption edge of Cu $L_{2,3}$ peaks shifted to the low-energy region under light, indicating the partial reduction of Cu. Notably, a new peak located at ≈934.7 eV was observed, which may result from the reordered energy levels of Cu 3*d* orbits. Based on the in situ sXAS results, we speculated that the photogenerated electrons excited from TiO_2 support transferred to Cu single atoms, and subsequently initiated the varies of Cu *d*-orbital energy levels location and components.

Density functional theory (DFT) calculations were performed to provide in-depth theoretical explanations for local coordination structure evolution of Cu single atoms and the reordered Cu 3*d*-orbital energy levels. Two optimized models denoted as Cu_1—O_4 and Cu_1—O_{2+1} were constructed with the reference from EXAFS analyses to simulate the states under darkness and light, respectively (Figure S23, Supporting Information). As for the central Cu atom in Cu_1—O_4, the vacancy formation energy of the surficial coordinated O atoms was lower than that of the internal axial coordinated O atom (Figure S24, Supporting Information). It enables the possibilities to realize the surficial oxygen defects generation with the light energy import, resulting in the conversion from the four-coordination to three-coordination structure. As for the total density of states analyses, a trap state composed with Cu-*d* orbit within the bandgap was observed in Cu_1—O_4 (Figure S25, Supporting Information). It suggests that the trap state in Cu_1—O_4 promoted the photogenerated electron transfer to Cu-*d* orbits and formed the electron-rich Cu single atoms in the Cu_1—O_{2+1} configuration, consistent with the differential charge density results. (Figure S26, Supporting Information). To further evaluate the effect of the electron transfer on Cu *d*-orbital energy levels, we conducted the projected density of states analyses. The 3*d*-orbital sequence of Cu_1—O_4 displays the main contribution of $d_{x^2-y^2}$ and d_{z^2} at the same energy position, while new mid-gap states emerged in Cu_1—O_{2+1} (Figure S27, Supporting Information). The variety of components in the *d*-orbital energy levels led to the different absorption peak splitting situation of Cu centers in Cu_1–O_4 and Cu_1–O_{2+1}. Specially, after photoactivation, the electron localization at the d_{z^2} orbit with the axial antibonding character caused the stretch of the axial Cu—O coordination (Figure S28, Supporting Information).[29,30]

Besides, Cu L-edge sXAS simulations according to the proposed coordination structure of the central Cu atom were performed. Evidently, the experimental spectra match well with the simulated profiles, confirming the local structural conversion of Cu single atoms under irradiation. After removing the light, the intermediate metastable structure with asymmetrical coordination reversibly restored to the previous state (Figures S29 and S30, Supporting Information). The experimental and theoretical studies reach a consensus that the external light field induced the reversible generation of the metastable asymmetrical Cu_1—O_{2+1} structure in Cu_1/TiO_2 (Figure 2e).

Considering the photo-responsive behaviors of Cu_1/TiO_2, we applied it in photocatalytic CO_2 reduction reaction. To assure the authenticity of photocatalytic CO_2 reduction process over catalysts, a series of controlled tests were first conducted (Table S2, Supporting Information). Then, we evaluated the catalytic performance of TiO_2 and Cu_1/TiO_2. CO and CH_4 were the main carbon-products over TiO_2, which achieved the yield rates of 10.1 and 3.6 μmol $g_{cat.}^{-1}$ h^{-1}, respectively (**Figure 3**a). After the decoration of Cu single atoms, the yield rates of CO and CH_4 displayed an obvious increase. More importantly, multi-carbon product of C_2H_4 was detected with the yield rate up to 60.4 μmol $g_{cat.}^{-1}$ h^{-1} over Cu_1/TiO_2, ranked among the best ever-reported photocatalysts for CO_2–to–C_2H_4 conversion (Table S3, Supporting Information). Evidently, the presence of atomically dispersed Cu sites induced the C—C coupling. Meanwhile, we measured the main by-product of H_2 over Cu_1/TiO_2 and calculated that the electron-based selectivity of C_2H_4 reached ≈75.2% (Figure S31, Supporting Information).

To further investigate the effect of the metastable structure of Cu_1–O_{2+1} to catalysis, we tracked the catalytic performance over Cu_1/TiO_2 underwent different pre-treatments in CO_2 reduction. In this process, we happened to find that the sequence of light treatment significantly influenced the yield of products. For clarity, the detailed procedure was specified (Table S4, Supporting Information). When Cu_1/TiO_2 was pre-treated in the dark and evaluated under CO_2 photoreduction conditions, the yield of C_2H_4 was first increased tardily, then tended to increase linearly along with the reaction time (Figure S32, Supporting Information). The yield rate of C_2H_4 also underwent the acceleration and the subsequent stable state (Figure 3b). When Cu_1/TiO_2 was exposed to light (denoted as photoactivation) before the reactants were further introduced, we recorded the yield of C_2H_4 during a 60-min photocatalytic CO_2 reduction reaction course (Figure S33, Supporting Information). The yield rate of C_2H_4 was almost stable with the time. The catalytic activity difference between the above conditions indicates that the light-induced metastable Cu_1–O_{2+1} worked as the real active structure promoted CO_2 photoreduction. It is worth noting that when Cu_1/TiO_2 was placed in the dark condition after been photoactivated, then participated in the reaction, the evolution of C_2H_4 over it underwent a similar course as the case over Cu_1/TiO_2 without photoactivation (Figure S34, Supporting Information). The experiment results suggest that the photo-induced stable–to–metastable structural conversion in Cu_1/TiO_2 was reversible, consistent with the in situ measurements.

Meanwhile, we designed an isotope labeling experiment and detected the products with synchrotron-based vacuum ultraviolet photoionization mass spectrometry (SVUV-PIMS). To avoid the complex fragment ions generated under the same high dissociation energy and obtain the high ionization cross section, different photon energies were selected for CO (14.2 eV), CH_4 (13.5 eV), and C_2H_4 (13.5 eV) analyses, respectively. With $^{13}CO_2$ as the purging gas, the peak sequences for ^{13}CO, $^{13}CH_4$, and $^{13}C_2H_4$ were detected over Cu_1/TiO_2, confirming that the carbon products generated in photocatalytic reaction originated from CO_2 (Figure 3c). To further determine the light utilization efficiency, we calculated the apparent quantum yield (AQY) of Cu_1/TiO_2 with the illumination of monochromatic light. At 365 nm, the AQY of Cu_1/TiO_2 attained 1.82% (Figure S35, Supporting

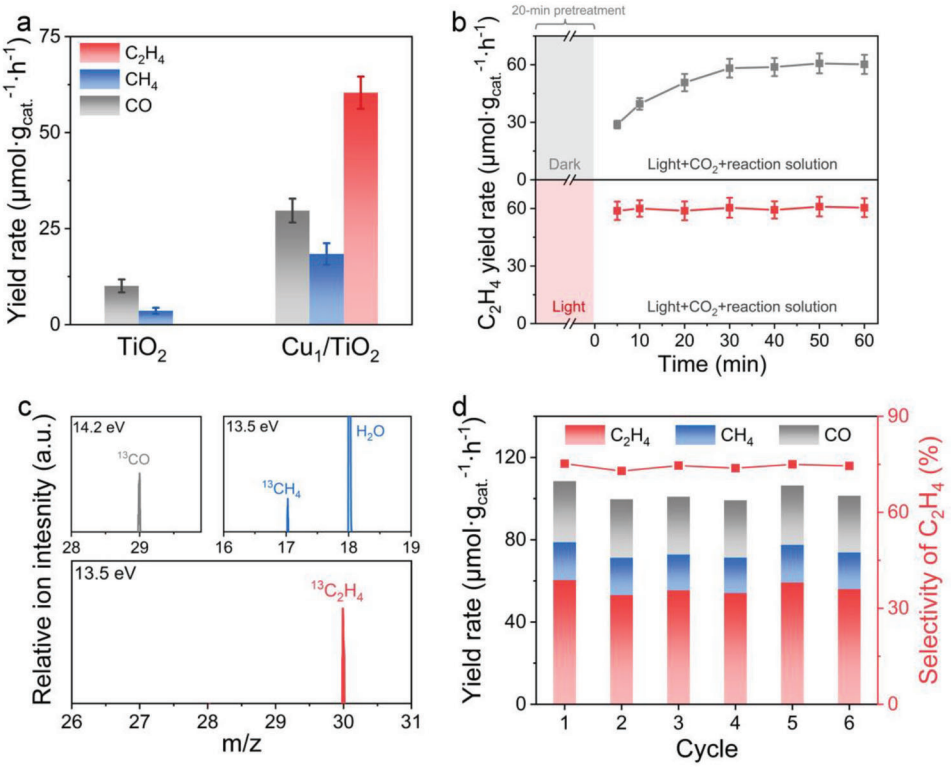

Figure 3. a) Products yield rates of TiO_2 and Cu_1/TiO_2 during photocatalytic CO_2 reduction. The error bars represent the standard deviation of three independent measurements. b) Time-dependent C_2H_4 yield rate over Cu_1/TiO_2 without (above) and with (below) photoactivation. c) SVUV-PIMS spectra for the products during $^{13}CO_2$ labeled photoreduction over Cu_1/TiO_2, detected at $h\nu = 14.2$ eV and $h\nu = 13.5$ eV, respectively. d) Cycling measurements for photocatalytic CO_2 reduction over Cu_1/TiO_2.

Information). Furthermore, we explored the stability of Cu_1/TiO_2. The initial activity was well-maintained after six successive reaction rounds, suggesting the high durability of Cu_1/TiO_2 photocatalysts (Figure 3d).

In order to monitor the impact of the photo-induced metastable active structure on the reactant molecule transformation, in situ diffuse reflectance infrared Fourier transform spectroscopy (DRIFTS) measurement was carried out. We recorded in situ DRIFTS spectra over Cu_1/TiO_2 under reaction conditions along with the prolonged irradiation time (**Figure 4**a). The characteristic peak at 1609 cm^{-1} was assigned to the *COOH group, which was the crucial intermediate for the formation of carbon-containing products.[31] The broad band centered at ≈2050 cm^{-1} corresponded to *CO.[32] The peak at 1063 cm^{-1} was attributed to *CHO.[33] Furthermore, through the successive hydrogenation of CHO, *CH_3O (1128 cm^{-1}) was generated as the intermediate of CH_4 products.[31] Meanwhile, the different vibration of C—H bond in CH or CH_2 groups (1452 cm^{-1}) authenticates the generation of CH_4 or C_2H_4.[32] Notably, the peak at 1025 cm^{-1} was attributed to the pivotal intermediates of C—COH for C_2 products.[32] And the gradually enhanced bands for *C_2H_4 (1689 and 1442 cm^{-1}) validates the generation of C_2H_4 over the active Cu_1—O_{2+1} structure in Cu_1/TiO_2.[34]

Additionally, we further compared the thermodynamics in the adsorption, activation, and transformation of reactant molecules over stable (Cu_1—O_4) and metastable structure (Cu_1—O_{2+1}), respectively. For the model of Cu_1–O_4, the adsorption energy (E_{ad}) of CO_2 molecule is −0.34 eV, while Cu_1—O_{2+1} is capable of adsorbing CO_2 molecule with a stronger adsorption energy of −0.83 eV (Figure 4b). Besides, the adsorption intensity of the significant intermediate of *CO is another factor to affect the CO_2 reduction performance, especially the product selectivity.[35] Evidently, *CO molecule is strongly adsorbed on the surface of Cu_1–O_{2+1} (−1.49 eV) rather than Cu_1—O_4 (−0.44 eV), conducing to the subsequent hydrogenation rather than CO desorption. Also, the reaction barriers of CO_2 reduction course over Cu_1–O_4 and Cu_1–O_{2+1} were depicted, respectively. The energy barrier of the first protonation step from CO_2 to *COOH shows an obvious decline over Cu_1–O_{2+1}, implying the stronger activation capability of the metastable asymmetrical structure to reactants (Figure 4c). Particularly, compared with Cu_1–O_4, Cu_1–O_{2+1} facilitates the C—C coupling process for further forming the C—C bonds. Be noted that, due to the strong interaction between Cu single atom and the TiO_2 substrate, the adjacent Ti atom acts as another site assists the Cu single atoms to accomplish the C—C coupling process. In brief, the thermodynamic advantages of Cu_1–O_{2+1} metastable structure endow it promising activity in CO_2 reduction reaction, also rationalized the spontaneous structural conversion.

3. Conclusion

In summary, we revealed that the light induced the reversible symmetry–to–asymmetry metastable state conversion and

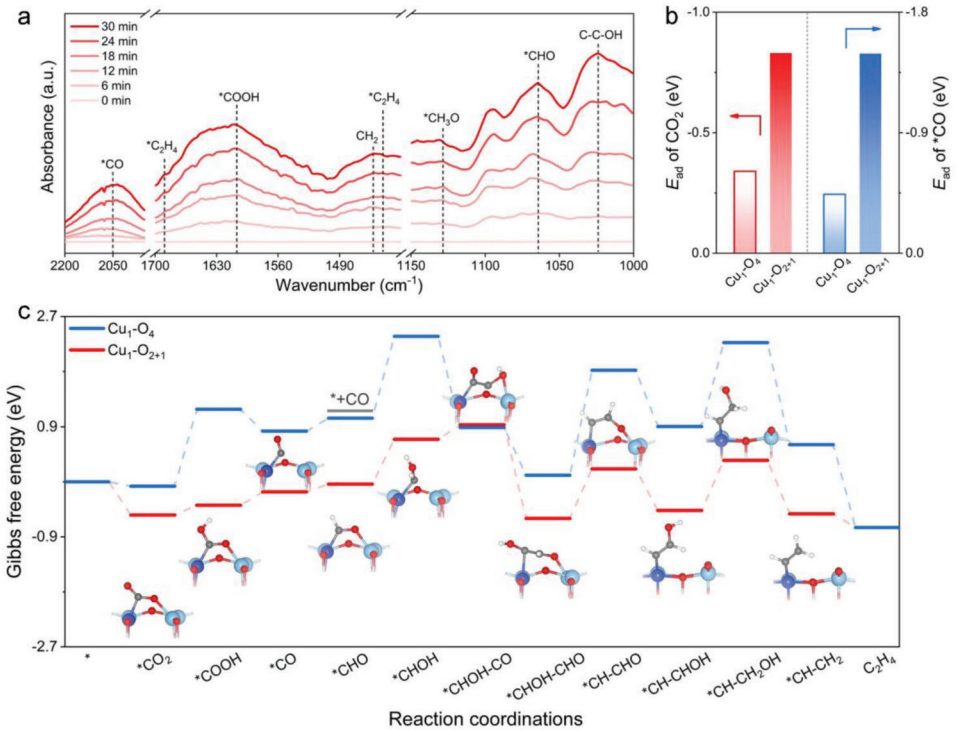

Figure 4. a) In situ DRIFTS spectra of Cu_1/TiO_2 during photocatalytic CO_2 reduction. b) The adsorption energies (E_{ad}) of CO_2 molecule (left axis) and CO* intermediate (right axis) on Cu_1–O_{2+1} and Cu_1–O_4, respectively. c) Gibbs free energy diagrams of the photocatalytic CO_2 reduction pathway over Cu_1–O_4 and Cu_1–O_{2+1}, respectively. The indigo, blue, red, grey, and white spheres represent Cu, Ti, O, C, and H atoms, respectively.

maintained the high-energy active metastable structure at Cu single-atom sites. As a result of the photogenerated electron transition to Cu-3*d* orbit, the *d*-orbital energy levels location and component were varied. The initial Cu_1–O_4 then distorted into Cu_1–O_{2+1} structure. During the photocatalytic CO_2 reduction, the presence of the real active structure of Cu_1–O_{2+1} contributed to the efficient CO_2 transformation. The main product of C_2H_4 achieved an impressive yield rate of 60.4 μmol $g_{cat.}^{-1}$ h^{-1}. Mechanistic investigations imply that the metastable Cu_1–O_{2+1} structure conduces to the stronger adsorption of reactant molecules and reduced the energy barrier. This work not only opens a feasible and low-energy consumption avenue for playing the catalytic value of the metastable structure, but also provides insightful understanding that local coordination environment affects catalytic performance.

4. Experimental Section

Chemicals and Materials: Copper(II) hexafluoroacetylacetonate hydrate ($Cu(hfac)_2$, 98%) was purchased from Shanghai Aladdin Bio-Chem Technology. Tetra-n-butyl titanate ($Ti(OBu)_4$·(TBOT), ≥99%), triethanolamine (TEOA, ≥99%), sodium hydroxide (NaOH, ≥99%), hydrofluoric acid solution (HF, 40%wt.%), ethanol (EtOH, ≥99%), and formalin (37% formaldehyde in an aqueous solution) were obtained from Sinopharm Chemical Reagent Co., Ltd. High purity carbon dioxide (CO_2, ≥99.999%), nitrogen (N_2, ≥99.999%), and Argon (Ar, ≥99.999%) were purchased from Nanjing Special Gas Factory Co. Ltd. $^{13}CO_2$ isotope (≥98%) was purchased from Wuhan Newradar Special Gas Co. Ltd. All solvents and chemicals were used without further purification. All aqueous solutions were prepared by using deionized (DI) water with a resistivity of 18.2 MΩ cm^{-1}.

Preparation of TiO_2: In a typical synthesis of TiO_2 nanosheets, 3 mL of HF solution was added into 25 mL of $Ti(OBu)_4$·(TBOT) under stirring for 2 h. Then the mixture was transferred into a 50-mL Teflon-lined autoclave, followed by being sealed and heated at 180 °C for 36 h. After cooling, the precipitate was collected by centrifugation, washed several times with ethanol and DI water. Afterwards, the precipitate was dispersed in 0.1 M NaOH solution and vigorously stirred at room temperature for 8 h. The products were collected by centrifugation, washed several times with ethanol and DI water, and then dried at 80 °C overnight.

Preparation of Cu_1/TiO_2: Cu_1/TiO_2 was obtained by ALD method. Typically, Cu ALD was carried out on the TiO_2 nanosheets in a viscous-flow stainless steel tube reactor system (ACME (Beijing) Technology) at 300 °C using $Cu(hfac)_2$ and formaldehyde as precursors. Ultrahigh purity N_2 (99.999%) was used as a carrier gas at a flow rate of 60 mL min^{-1}. $Cu(hfac)_2$ precursor was heated to 65 °C to meet the sufficient vapor pressure. The precursor inlet lines were heated to 100 °C to prevent condensation of the Cu precursor. The timing sequence was 300, 300, 40, and 180 s for $Cu(hfac)_2$ exposure, N_2 purge, formaldehyde exposure, and N_2 purge, respectively.

Photoelectrochemical Measurement: First, the original FTO glasses were cleaned with ethanol by ultrasonic treatment for 30 min. 5.0 mg of as-obtained catalysts was dispersed in 0.5 mL of terpineol followed by ultrasound for 2 h. The acquired suspension was added onto a 1 cm × 1 cm FTO glass. Noting that another drop of the suspension was added after the previous one dried up. Before photoelectrochemical measurements, the FTO glasses were treated in vacuum at 80 °C for 2 h. The experiments were carried out on the electrochemical station of CHI 660E at room temperature. Standard three-electrode setup was used with the FTO glass coated with catalysts as the working electrode, a Pt foil as the counter electrode, and an Ag/AgCl electrode as the reference electrode. 0.5 M Na_2SO_4 aqueous solution was employed as the electrolyte.

In Situ XAS Measurements: X-ray absorption spectra at Cu K-edge (E_0 = 8979 eV) was performed at beamline BL14W1 of Shanghai Synchrotron Radiation Facility (SSRF) operated at 3.5 GeV under "top-up" mode with a constant current of 220 mA. The Cu K-edge spectrum of Cu_1/TiO_2 was recorded under fluorescence mode with a Lytle chamber. The white light was monochromatized by a Si (111) double-crystal monochromator. During the in situ XAS data collection, the sample was under light irradiation of the optical fiber. Athena and Artemis codes were used to extract and fit data. For the XANES part, the experimental absorption coefficients as a function of energies μ(E) were processed by background subtraction and normalization procedures. This process is referred as "normalized absorption". The EXAFS spectra were obtained by subtracting the post-edge background from the overall absorption and then normalizing with respect to the edge-jump step. For the EXAFS part, the Fourier-transformed (FT) data were fitted in R space. The passive electron factor, S_0^2, was determined by fitting the experimental Cu foil data, and then fixed for further analysis of the measured samples. The parameters describing the local structure environment including coordination number (*CN*), bond distance (*R*), and Debye-Waller (*DW*) factor around the absorbed atoms were allowed to vary during the fit process. Wavelet transform (WT) analysis was employed using the Igor pro script developed by Funke et al.[36] The Morlet wavelet was chosen as basis mother wavelet and the parameters ($\eta = 8$, $\sigma = 1$) were used for a better resolution in the wave vector *k*.

In Situ sXAS Measurements: In situ sXAS measurements were performed at the photoemission end-station at beamline BL10B of National Synchrotron Radiation Laboratory (NSRL) in Hefei, China. The beamline is connected to a bending magnet and covers photon energies from 100 to 1,000 eV with a resolving power (E/ΔE) better than 1000 and the photon flux is 1×10^9 photons per second. In situ sXAS tests were recorded under the irradiation through the window of the analysis chamber. The sXAS raw data was first calibrated from Au 4*f* peak as a standard. Then, the pre-edge of substrate was set to be 0. The edge-jump of the as-obtained spectra was normalized to be 1. The quantitative analysis of Cu L-edge sXAS spectra was performed using the FDMNES package, which is capable of quantitatively analyzing the XANES spectrum from the absorption edge up to ≈50 eV via comparison between experimental data and theoretical calculations obtained by changing relevant geometrical parameters around the photon absorber site. The X-ray absorption cross-sections were calculated using the full multiple scattering approach in the framework of the muffin-tin (MT) approximation for the shape of the potential. In this case, spectra typically converge when the cluster includes 25 atoms within a radius of 6.0 Å.

Catalytic Tests: In a typical catalytic test, 20 mg of photocatalysts and 20 mL of DI water were added into a photoreactor, which was then bubbled with pure CO_2 at a flow rate of 30 mL min^{-1} for 30 min. TEOA was also added into the reactor as the sacrificial agent. Subsequently, the suspension was irradiated by a Xenon lamp (Beijing Perfectlight PLS-SXE300D) under full-spectrum with continuous stirring. The reactor was kept at room temperature via circulation cooling water during reaction process. After the completion of reaction, the generated C_2H_4, CH_4, CO, H_2, and O_2 were analyzed by gas chromatography (GC-2014C, SHIMADZU) with a flame ionization detector (FID) and a thermal conductivity detector (TCD). The isotope-labeling experiments of $^{13}CO_2$ were analyzed by the synchrotron-based vacuum ultraviolet photoionization mass spectrometry (SVUV-PIMS) was carried out at the mass spectrometry end-station (BL04B) beamline of NSRL in Hefei, China. To test the recycling stability of Cu_1/TiO_2, the first measurement was conducted as described above. Then, the suspension was immediately centrifuged at 8000 rpm for 10 min and washed with DI water several times. Subsequently, the sediment was applied as the photocatalyst in the next catalytic cycle.

Measurements of Apparent Quantum Yield (AQY): The catalytic reactions for determining AQY were carried out in a quartz topirradiation-type reaction vessel. The value of AQY was calculated through the following equation:

$$\mathrm{AQY} = \frac{N_e}{N_p} = \frac{12N_{C_2H_4}}{N_p} \times 100\% \quad (1)$$

$$N_p = \frac{W \cdot A \cdot t}{h \cdot \nu} \quad (2)$$

N_e, N_p, and N_{C2H4} represent the number of reacted electrons, incident photons, generated C_2H_4, respectively. ν, *W*, *A*, and *t* are the incident light frequency, intensity, irradiation area, and reaction time, respectively.

In Situ DRIFTS Measurements: In situ DRIFTS measurements were performed at the infrared spectroscopy and microspectroscopy end-station (BL01B) of National Synchrotron Radiation Laboratory (NSRL) in Hefei, China. The data was collected by using a Bruker IFS 66v Fourier-transform spectrometer equipped with a Harrick diffuse reflectance accessory. The in situ chamber was equipped with two ZnSe windows for synergetic light illumination. Each spectrum was recorded by averaging 128 scans at a 2 cm^{-1} spectral resolution.

DFT Calculations: All computations in present work have been performed by Vienna ab initio Simulation Package (VASP) with the projector-augment-wave (PAW) method.[37,38] The electron exchange and correlation were described by the generalized gradient approximation (GGA) with the function of revised Perdew-Burke-Ernzerhof (PBE).[39] The cut-off energy was set up to 500 eV. The force convergence was set to be lower than 0.02 eV $Å^{-1}$, and the total energy convergence was set to be smaller than 10^{-5} eV. Electron smearing of $\sigma = 0.05$ eV was used following the Gaussian scheme. The Brillouin zone was sampled using Monkhorst–Pack scheme with a *k*-point mesh of $3 \times 3 \times 1$ centered at the Γ-centered point for the structural relaxation, and $3 \times 3 \times 1$ k-point mesh was used for the static calculations of charge density difference, $6 \times 6 \times 1$ k-point mesh was used for the static calculations of density of states and VASPMO.[40] The energy of 10^{-5} eV and force convergence criteria of −0.02 eV/Å were used to realize the atomic relaxation. The calculated anatase TiO_2 bulk lattice parameters of $a = b = 3.90$ Å and $c = 9.59$ Å. U_{eff} = 4.2 and 5.2 eV were applied to the Ti 3*d* and Cu 3*d* electrons. The slab model of anatase TiO_2 (001) surface contains 4 atomic layers (48 atoms) in thickness with 2 bottom layers fixed while relaxing other atoms besides. The vacuum slab was set up to 15 Å. All the Gibbs free energy (ΔG) calculations were corrected at 298.15 K by the VASPKIT program.

Instrumentations: SEM images were collected on a FEI XL-30 ESEM scanning electron microscope operated at 5 kV. HAADF-STEM images were collected on a JEOL ARM-200F field-emission transmission electron microscope operating at 200 kV accelerating voltage. The content of Cu was quantified by an Optima 7300 DV inductively-coupled plasma atomic emission spectrometer (ICP-AES). Powder XRD patterns were recorded by using a Philips X'Pert Pro Super X-ray diffractometer with Cu-Kα radiation (λ = 1.54178 Å). The UV-vis diffuse reflectance spectra were recorded on a UV–*vis*-NIR spectrophotometer (Perkin Elmer Lambda 950). X-ray photoemission spectroscopy was performed at the photoemission end-station (BL10B) beamline of National Synchrotron Radiation Laboratory (NSRL) in Hefei, China. The XPS database (NIST X-ray Photoelectron Spectroscopy Database, https://srdata.nist.gov/xps/intro.aspx) was used as a reference to assign the possible chemical states. The ultraviolet photoelectron spectroscopy was performed at the catalysis and surface science end-station (BL11U) beamline of National Synchrotron Radiation Laboratory (NSRL) in Hefei, China. The incident photon energy was 40 eV.

Supporting Information

Supporting Information is available from the Wiley Online Library or from the author.

Acknowledgements

Q.W., Y.Z., and M.L. contributed equally to this work. This work was supported by National Natural Science Foundation of China (Grant Nos. 1222508, U1932213, and U21A20317), the Fundamental Research Funds for the Central Universities (Nos. WK2060000016), the USTC Research Funds of the Double First-Class Initiative (Nos. YD2310002005 and YD9990002014), Natural Science Foundation of Anhui Province

(2208085QB42), the Youth Innovation Promotion Association CAS (2020454). The authors thank the beamline BL14W1 in SSRF, BL10B, BL04B, and BL01B in NSRL for synchrotron radiation measurements. The calculations were conducted on the supercomputing system in the Supercomputing Center of USTC.

Conflict of Interest

The authors declare no conflict of interest.

Data Availability Statement

The data that support the findings of this study are available from the corresponding author upon reasonable request.

Keywords

Cu single atom, ethylene, metastable asymmetric structure, photocatalytic CO_2 reduction, photoinduced structural evolution

Received: August 15, 2023
Revised: September 12, 2023
Published online: September 24, 2023

[1] J. Hong, J.-H. Bae, H. Jo, H.-Y. Park, S. Lee, S. J. Hong, H. Chun, M. K. Cho, J. Kim, J. Kim, Y. Son, H. Jin, J.-Y. Suh, S.-C. Kim, H.-K. Roh, K. H. Lee, H.-S. Kim, K. Y. Chung, C. W. Yoon, K. Lee, S. H. Kim, J.-P. Ahn, H. Baik, G. H. Kim, B. Han, S. Jin, T. Hyeon, J. Park, C. Y. Son, Y. Yang, et al., *Nature* **2022**, *603*, 631.
[2] M. H. Cohen, D. Turnbull, *Nature* **1964**, *203*, 964.
[3] W. Sun, S. T. Dacek, S. P. Ong, G. Hautier, A. Jain, W. D. Richards, A. C. Gamst, K. A. Persson, G. Ceder, *Sci. Adv.* **2016**, *2*, e1600225.
[4] Z. Lai, Q. He, T. H. Tran, D. V. M. Repaka, D.-D. Zhou, Y. Sun, S. Xi, Y. Li, A. Chaturvedi, C. Tan, B. Chen, G.-H. Nam, B. Li, C. Ling, W. Zhai, Z. Shi, D. Hu, V. Sharma, Z. Hu, Y. Chen, Z. Zhang, Y. Yu, X. Renshaw Wang, R. V. Ramanujan, Y. Ma, K. Hippalgaonkar, H. Zhang, *Nat. Mater.* **2021**, *20*, 1113.
[5] Z. Ji, W. Yuan, S. Zhao, T. Wang, S. Umer, S. Ding, J. Liu, J. Liu, Y. Zhao, W. Hu, *Chem Catal* **2023**, *3*, 100529.
[6] E. K. Abo-Hamed, T. Pennycook, Y. Vaynzof, C. Toprakcioglu, A. Koutsioubas, O. A. Scherman, *Small* **2014**, *10*, 3145.
[7] Z. Wang, J. Chen, E. Song, N. Wang, J. Dong, X. Zhang, P. M. Ajayan, W. Yao, C. Wang, J. Liu, J. Shen, M. Ye, *Nat. Commun.* **2021**, *12*, 5960.
[8] X. Tan, S. Geng, Y. Ji, Q. Shao, T. Zhu, P. Wang, Y. Li, X. Huang, *Adv. Mater.* **2020**, *32*, 2002857.
[9] M. Chen, Y. Yan, M. Gebre, C. Ordonez, F. Liu, L. Qi, A. Lamkins, D. Jing, K. Dolge, B. Zhang, P. Heintz, D. P. Shoemaker, B. Wang, W. Huang, *Angew. Chem., Int. Ed.* **2021**, *60*, 18309.
[10] Y.-C. Lin, D. O. Dumcenco, Y.-S. Huang, K. Suenaga, *Nat. Nanotechnol.* **2021**, *9*, 391.
[11] B.-R. Chen, W. Sun, D. A. Kitchaev, J. S. Mangum, V. Thampy, L. M. Garten, D. S. Ginley, B. P. Gorman, K. H. Stone, G. Ceder, M. F. Toney, L. T. Schelhas, *Nat. Commun.* **2018**, *9*, 2553.
[12] Y. Kang, S. Najmaei, Z. Liu, Y. Bao, Y. Wang, X. Zhu, N. J. Halas, P. Nordlander, P. M. Ajayan, J. Lou, Z. Fang, *Adv. Mater.* **2014**, *26*, 6467.
[13] Z. Zhang, J. Yu, J. Zhang, Q. Ge, H. Xu, F. Dallmann, R. Dittmeyer, J. Sun, *Chem. Sci.* **2018**, *9*, 3386.
[14] W. Wen, P. Yan, W. Sun, Y. Zhou, X.-Y. Yu, *Adv. Funct. Mater.* **2023**, *33*, 2212236.
[15] M.-G. Kim, M. G. Kanatzidis, A. Facchetti, T. J. Marks, *Nat. Mater.* **2011**, *10*, 382.
[16] K. K. Banger, Y. Yamashita, K. Mori, R. L. Peterson, T. Leedham, J. Rickard, H. Sirringhaus, *Nat. Mater.* **2011**, *10*, 45.
[17] Y. Zhao, Y. Zhao, G. I. N. Waterhouse, L. Zheng, X. Cao, F. Teng, L.-Z. Wu, C.-H. Tung, D. O'hare, T. Zhang, *Adv. Mater.* **2017**, *29*, 1703828.
[18] X. Lu, M. Yu, G. Wang, T. Zhai, S. Xie, Y. Ling, Y. Tong, Y. Li, *Adv. Mater.* **2013**, *25*, 267.
[19] S. Zhang, Y. Zhao, R. Shi, C. Zhou, G. I. N. Waterhouse, L.-Z. Wu, C.-H. Tung, T. Zhang, *Adv. Energy Mater.* **2020**, *10*, 1901973.
[20] Y. Zhang, Q. Wang, S. Yang, H. Wang, D. Rao, T. Chen, G. Wang, J. Lu, J. Zhu, S. Wei, X. Zheng, J. Zeng, *Adv. Funct. Mater.* **2022**, *32*, 2112452.
[21] Q. Wang, Y. Xiao, S. Yang, Y. Zhang, L. Wu, H. Pan, D. Rao, T. Chen, Z. Sun, G. Wang, J. Zhu, J. Zeng, S. Wei, X. Zheng, *Nano Lett.* **2022**, *22*, 10216.
[22] E. V. Golubina, E. S. Lokteva, A. V. Erokhin, A. A. Veligzhanin, Y. V. Zubavichus, V. A. Likholobov, V. V. Lunin, *J. Catal.* **2016**, *344*, 90.
[23] I. A. Pankin, A. Martini, K. A. Lomachenko, A. V. Soldatov, S. Bordiga, E. Borfecchia, *Catal. Today* **2020**, *345*, 125.
[24] Y. Liu, L. Tian, X. Tan, X. Li, X. Chen, *Sci. Bull.* **2017**, *62*, 431.
[25] C. Liu, J. Qian, Y. Ye, H. Zhou, C.-J. Sun, C. Sheehan, Z. Zhang, G. Wan, Y.-S. Liu, J. Guo, S. Li, H. Shin, S. Hwang, T. B. Gunnoe, W. A. Goddard, S. Zhang, *Nat. Catal.* **2021**, *4*, 36.
[26] A. Braun, K. K. Akurati, G. Fortunato, F. A. Reifler, A. Ritter, A. S. Harvey, A. Vital, T. Graule, *J. Phys. Chem. C* **2010**, *114*, 516.
[27] Y. Yang, L. C. Kao, Y. Liu, K. Sun, H. Yu, J. Guo, S. Y. H. Liou, M. R. Hoffmann, *ACS Catal.* **2018**, *8*, 4278.
[28] K.-I. Shimizu, H. Maeshima, H. Yoshida, A. Satsuma, T. Hattori, *Phys. Chem. Chem. Phys.* **2001**, *3*, 862.
[29] J. Han, P. An, S. Liu, X. Zhang, D. Wang, Y. Yuan, J. Guo, X. Qiu, K. Hou, L. Shi, Y. Zhang, S. Zhao, C. Long, Z. Tang, *Angew. Chem., Int. Ed.* **2019**, *58*, 12711.
[30] B.-H. Lee, S. Park, M. Kim, A. K. Sinha, S. C. Lee, E. Jung, W. J. Chang, K.-S. Lee, J. H. Kim, S.-P. Cho, H. Kim, K. T. Nam, T. Hyeon, *Nat. Mater.* **2019**, *18*, 620.
[31] X.-L. Gong, H.-Q. Lu, K. Li, W. Li, *Sep. Purif. Technol.* **2022**, *286*, 120478.
[32] W. Gao, S. Li, H. He, X. Li, Z. Cheng, Y. Yang, J. Wang, Q. Shen, X. Wang, Y. Xiong, Y. Zhou, Z. Zou, *Nat. Commun.* **2021**, *12*, 4747.
[33] Y. Wu, Q. Chen, J. Zhu, K. Zheng, M. Wu, M. Fan, W. Yan, J. Hu, J. Zhu, Y. Pan, X. Jiao, Y. Sun, Y. Xie, *Angew. Chem., Int. Ed.* **2023**, *62*, e202301075.
[34] Y. Yu, X. '. Dong, P. Chen, Q. Geng, H. Wang, J. Li, Y. Zhou, F. Dong, *ACS Nano* **2021**, *15*, 14453.
[35] A. Vasileff, C. Xu, Y. Jiao, Y. Zheng, S.-Z. Qiao, *Chem* **2021**, *15*, 14453.
[36] H. Funke, A. C. Scheinost, M. Chukalina, *Phys. Rev. B* **2005**, *71*, 094110.
[37] G. Kresse, J. Furthmüller, *Phys. Rev. B* **1996**, *54*, 11169.
[38] G. Kresse, D. Joubert, *Phys. Rev. B* **1999**, *59*, 1758.
[39] J. P. Perdew, K. Burke, M. Ernzerhof, *Phys. Rev. Lett.* **1996**, *77*, 3865.
[40] S. Grimme, J. Antony, S. Ehrlich, H. Krieg, *J. Chem. Phys.* **2010**, *132*, 154104.